Modeling of Rayleigh Scattering Imaging of Detonation Waves: Quantum Computation of Rayleigh Cross-Sections and Real Diagnostic Effects

G. Bechon[1,2]; R. Mével[1,*]; D. Davidenko[3,4], J.E. Shepherd[1]

[1]Graduate Aeronautical Laboratories, California Institute of Technology, Pasadena, USA
[2]Ecole Polytechnique, Paris, France
[3]ICARE-CNRS, Orléans, France
[4]ONERA, Palaiseau, France

Corresponding author: mevel@caltech.edu

Abstract

A detailed Rayleigh scattering model has been implemented and used to post-process detonation wave numerical simulation results to allow for a direct comparison with previous experimental visualizations of detonations in hydrogen-based mixtures. A quantum chemistry approach has been employed to obtain realistic Rayleigh scattering cross-sections. A database of Rayleigh cross-sections for relevant species was created and validated against available experimental data. Steady one-dimensional as well as unsteady two-dimensional simulations of detonation were used for comparison with experimental Rayleigh profiles and images. We demonstrate that both realistic Rayleigh scattering cross-sections and the characteristics of the imaging system have to be taken into account to accurately reproduce the experimental results. We show how this approach can be applied to estimate the performance and design improved Rayleigh imaging systems. Rayleigh scattering appears to offer some advantages over other techniques for studying the structure of detonation waves both at and behind the front.

Keyword: Detonation Structure; Rayleigh scattering; DFT method

PACS: 01.50.Kw; 47.15.Pn; 47.40.Rs

1

1 Introduction

Detonations are a shock wave-reaction zone complex that travels at a supersonic speed. The energy released by the chemical reactions sustains the shock wave propagation which in turn initiates the auto-ignition of the gaseous mixture [1–3]. Research on detonation has been motivated by propulsion applications as well as industrial safety [3]. The detonation structure has been extensively studied using density-based visualization techniques such as interferometry [4, 5] and schlieren [6–9]. The disadvantage of these techniques is that the density gradients are integrated over one dimension of the investigated volume [10] which makes the interpretation of the results difficult or requires the use of narrow channels which induce a modification of the detonation wave structure [11]. During the last three decades, the development of a variety of laser light sources as well as sensitive imaging systems have enabled two-dimensional imaging of detonation based on spectroscopic processes. Anderson and Dabora [12, 13] performed Rayleigh scattering imaging of detonation waves propagating in hydrogen-based mixtures. The work was succesful in demonstrating the potential of the technique but the resolution of imaging system and low light levels resulted in low signal-to-noise ratio. There has been no further studies with Rayleigh scattering in detonation although it is widely used in other fluid dynamic and combustion experiments [14–21]. A number of authors including Kamel et al. [22], Viguier et al. [23], Wang et al. [24], Austin et al. [11, 25] and Pintgen et al. [10, 26–28] have used OH radical laser-induced fluorescence to visualize the geometry of the reaction zone of detonation in a wide range of mixtures. The work of Austin et al. [11, 25] and Pintgen et al. [10, 26–28] was recently continued by Mével et al. [29] who developed a detailed laser induced fluorescence model to post-process numerical simulation results on detonation waves, allowing for a direct comparison between the experimental and numerical images. It was demonstrated that the strong attenuation of the incident laser light, due to the strong absorption at the detonation front, prevented imaging regions of high OH concentration away from the front. Rayleigh scattering imaging is potentially less susceptible to absorption and might be an appropriate method to reconsider for detonations imaging considering the improvements in technology since the study of Anderson and Dabora in 1992. To accurately estimate the possibilities and limitations of this technique, we have undertaken a detailed analysis of the Rayleigh scattering process in detonations.

In the present study, an ab initio quantum chemistry approach has been employed to develop a wavelength and temperature-dependent Rayleigh scattering cross-section database. After its validation against the data from the literature, this

database was used to post-process one- and two-dimensional detonation simulations in order to compute the Rayleigh scattering intensity of a detonation wave. These simulations were compared to Rayleigh images obtained by Anderson and Dabora [12]. Estimates of the capability of a contemporary imaging system are made using realistic performance parameters to determine the feasability of imaging features close to and far behind the detonation front.

2 Rayleigh scattering cross-section database

2.1 Fundamentals of Rayleigh scattering

The fundamental principle governing Rayleigh scattering is the elastic interactions between gas molecules and incident laser light [15–17]. The Rayleigh scattering intensity I_{Ray} can be defined as the number of photons per second diffused by a volume V of gas, and collected within the solid angle Ω along an axis perpendicular to the direction of propagation of the incident light and the direction of its polarization [17, 30]:

$$I_{Ray} = k \Omega V I_{0,S} N \frac{\partial \sigma}{\partial \Omega} \tag{1}$$

where $I_{0,S}$ is the intensity of the incident light in $photon \cdot s^{-1} \cdot m^{-2}$, N the density number and k is a system calibration constant which accounts for the optical collection and transmission efficiencies. In order to compute the Rayleigh intensity, the density and the Rayleigh differential cross-section are needed.

The differential cross-section depends on the position of the detector, the wavelength λ, of the laser light, and the optical properties of the gas [31]. It can be calculated using the approximation

$$\frac{\partial \sigma}{\partial \Omega} \approx \frac{4\pi^2 (n-1)^2}{\lambda^4 N^2} \sin^2 \phi \frac{3}{3 - 4\rho} \tag{2}$$

where N is the density number, ϕ is the angle of refraction defined as the angle between the polarization direction and the observation direction, ρ is the depolarization factor

$$\rho = \frac{6\gamma^2}{45a^2 + 7\gamma^2}, \tag{3}$$

with the linear polarizability

$$a^2 = \frac{1}{9}(\alpha_{11} + \alpha_{22} + \alpha_{33})^2, \tag{4}$$

and the anisotropy

$$\gamma^2 = \frac{1}{2}\{(\alpha_{11} - \alpha_{22})^2 + (\alpha_{22} - \alpha_{33})^2 + (\alpha_{33} - \alpha_{11})^2 + 6(\alpha_{12}^2 + \alpha_{23}^2 + \alpha_{31}^2\}. \quad (5)$$

α_{ij} are the polarizability tensor elements.

To simplify this equation, the case $\phi = \frac{\pi}{2}$, where the differential cross-section is maximum, is usually considered. Using the Lorenz-Lorentz equation to replace the index of refraction by the linear polarizability we obtain:

$$\frac{\partial \sigma}{\partial \Omega} \approx \frac{16\pi^4}{\lambda^4}a^2 F \quad (6)$$

with

$$F = \frac{3}{3 - 4\rho} \approx 1 + \frac{7\gamma^2}{45a^2} \quad (7)$$

the King factor and a the linear polarizability in m^3.

Considering a mixture of gaseous species, the total cros-section is an average over the individual species values [31]:

$$\frac{\partial \sigma}{\partial \Omega} = \sum_{i=1}^{n} X_i \frac{\partial \sigma_i}{\partial \Omega} \quad (8)$$

where X_i is the molar fraction of the species i.

2.2 Creation and validation of the database

The database was created using the quantum chemistry software *Gaussian03* [32], which can compute wavelength dependent polarizability tensor that is needed for computing the Rayleigh cross-sections. The database contains the complete polarizability tensor at 12 different wavelengths for 30 species. Two basis sets were compared: the *6-311+G(3df,2p)* and the *aug-cc-pVTZ* basis set. They differ from each other through the number and nature of diffuse and polarization functions used to describe the atomic and valence orbitals. The two basis sets were compared using the experimental refractivity data collected by Gardiner et al. [33] in the range 337-694 *nm*. The relationship between refractivity, R_L, and polarizability is:

$$R_L = a\frac{N_A}{3\varepsilon_0} \quad (9)$$

where N_A is the Avogadro number and ε_0: is the vacuum permittivity.

The geometry of the molecule was optimized for each theory level-basis set combination, then the polarizability tensor was calculated. Comparison with the data was made for 26 species. The relative error for all species and the two different basis sets is shown in Figure 1. For most species, the *aug-cc-pVTZ* basis set enables a better prediction of the refractivity than the *6-311+G(3df,2p)* basis set. Considering the 26 species, the mean relative error is 15% for the *6-311+G(3df,2p)* against 10% for the *aug-cc-pVTZ*. For the species of the H_2-O_2 chemical system, the mean error is 31% for *6-311+G(3df,2p)* and 13% for the *aug-cc-pVTZ* basis set. Consequently, the *B3LYP/aug-cc-pVTZ* method was employed to create the Rayleigh cross-section database.

In addition to Gardiner et al. [33] refractivity data, the depolarization ratio data of Fielding et al. [34] and the cross-section data of Sutton and Driscoll [35] were used to validate the Rayleigh cross-section database. An overview of these comparisons is displayed in Figure 2. Both for Fielding et al. and Sutton and Driscoll data, overall agreement was found with an average error on the order of 10%. The Rayleigh scattering cross-section database which includes 33 chemical species is provided as a supplemental material.

Since the temperature variations in a detonation wave are significant, it is important to account for the temperature dependance of the cross-sections. As *Gaussian* does not permit compution of a temperature-dependent polarizability tensor, we analysed the results of Sutton and Driscoll [35], Zhao and Hiroyasu [17], Graham et al. [36] and Holm and Kerl [37], to establish a wavelength dependent relationship for the relative variation of the cross-section with temperature, $\Delta\sigma_T$. We note that

- Sutton and Driscoll in their work measured cross-sections for 7 species (N_2, Ar, O_2, CO_2, CO, H_2 and CH_4) at different temperatures for two wavelengths: 266 and 355 *nm*. They found that the variation of the cross-section between 300 and 1500 *K* was less than 8% at 355 *nm* and less than 11% at 266 *nm*.

- Zhao and Hiroyasu, and Graham et al., considered in their studies that the estimated relative change of cross-section of methane, and simple molecules like N_2, O_2, CO_2, CO, due to temperature is approximately constant and equal to $2 \times 10^{-5} K^{-1}$ which leads to less than 4% of change on the cross-section between 300 and 1500 *K*.

5

- Holm and Kerl determined by interferometry (at 546 *nm*) the index of refraction of 5 gases (He, Ar, H_2, N_2 and O_2) between 208 and 365K. After correction, they obtained for H_2, N_2 and O_2 $\Delta\sigma_T = 2 \times 10^{-5}K^{-1}$. If this relative change is assumed constant over temperature, as it is found in the Sutton and Driscoll analysis, a change of less than 4% on the cross section is expected between 300 and 1500 K.

From these results, it can be concluded that the changes of σ with temperature are small, that $\Delta\sigma_T$ does not depend on temperature and the wavelength dependence is important

$$\Delta\sigma_T(546nm) \approx 2 \times 10^{-5}K^{-1} \tag{10}$$

$$\Delta\sigma_T(355nm) \approx 5 \times 10^{-5}K^{-1} \tag{11}$$

$$\Delta\sigma_T(266nm) \approx 8 \times 10^{-5}K^{-1} \tag{12}$$

Subsequently, we assumed that the temperature dependence of the Rayleigh scattering cross-section is constant with temperature. We also assumed that the wavelength dependence can be extrapolated to a wider range of wavelengths [250 *nm*, 700 *nm*] as illustrated in Figure 3. The variation of the Rayleigh scattering cross-section with temperature over the range 300-2000 K is thus given by:

$$\sigma_T^i(\lambda) = \sigma_0^i(\lambda) \cdot [1 + \Delta\sigma_T(\lambda) \cdot (T - T_0)] \tag{13}$$

with σ_0^i the cross-section of the *i* species at T_0=298 K.

3 Application to detonation simulations

3.1 Detonation models

Two detonation modeling approaches have been employed in the present study: the steady one-dimensional model, or ZND model [38], and unsteady two-dimensional simulations. The ZND model considers the detonation wave to be composed of a steady one-dimensional planar shock wave followed by a reaction zone [1]. Shock wave theory is used to determine the flow conditions behind a normal shock. For the reaction zone, a system of ordinary differential equations, derived from Euler equations for 1-D steady flow, is solved. The detonation speed in the Chapman-Jouguet mode is determined to obtain a sonic flow at the end of the reaction zone. The shock wave induces the auto-ignition of the combustible mixture and, in

turn, the expansion of the gases sustains the wave propagation. Unsteady two-dimensional cellular detonations were simulated by solving the Euler equations with a high-resolution computer code based on the finite-difference method. For the numerical flux approximation, the shock capturing, weighted essentially non-oscillatory (WENO) scheme of the fifth order [39] is employed along with the Lax-Friedrichs splitting of fluxes in the characteristic form. For the time integration, the ASIRK2C second-order semi-implicit additive Runge-Kutta scheme [40] is used. The convective terms in the Euler equations are treated explicitly while the implicit treatment is applied to the chemical source terms. Details about the computational domain, boundary conditions and validation process of the code can be found in [29, 41].

Calculations were made using the detailed reaction model of Mével et al. [42–44] which was validated against a wide range of experimental data including shock-tube, flow and jet-stirred reactor, and laminar burning speed data, as described in detail in Mével[45].

3.2 Rayleigh imaging

In order to understand the relationship between the experimental and calculated Rayleigh images, we investigated the effects of the characteristics of the imaging system, such as the resolution of the camera, the spatial distribution of the laser sheet and the dynamic range of the camera. In addition, the possible attenuation of the laser light intensity has also been studied. We considered a 3 mm diameter laser beam with a wavelength of 266 nm (as in Anderson and Dabora's study [12]), fourth harmonic of a Nd-Yag laser, which is used to create a 30 mm wide laser sheet with a thickness of 0.5 mm. The incident intensity is 55 kJ/m^2. A lens with a f number of 2.8 is used to image the detonation with a magnification of 2 onto a UV sensitive CCD array located 20 cm away. The overall efficiency of the optical system, including the quantum efficiency of the CCD and the transmission of the interference bandpass filter, is chosen to be 10%. This value was taken based on the typical efficiency of UV pass-band filters, transmission peak of 30%, and ICCD cameras with a quantum efficiency of 30%. Simulation results of a 2-D detonation in a 2H$_2$-O$_2$-12Ar at P$_1$=20 kPa and T$_1$=295 K were used to generate synthetic Rayleigh scattering images.

Figure 4 illustrates the effects of the characteristics of the imaging system. Figure 4 a) shows the base-image which has been obtained considering a camera resolution of 32 μm which corresponds to the grid size used to perform the det-

7

onation simulation. The effects of resolution is illustrated in Figure 4 b) and c). In Figure 4 b), a resolution of 70 μm was considered. In Figure 4 c), the effect of averaging over a number of pixels (here 10 px) to increase the signal-to-noise ratio is illustrated. In addition, the effect of imaging system (using a point spread function as described by Clemens [46]) was also investigated considering a magnification of 4 and a lens with a focal number of 22. These three effects spread out the region of high intensity scattering and blur the separation between high and low intensity regions. The small length-scale features are less visible and the intensity distribution in certain zones behind the front is modified.

The effect of the attenuation of the incident laser light as it travels through the detonation front is illustrated in Figure 4 d). In order to observe an effect, the Rayleigh scattering cross-sections had to be multiplied by 10^6. This is consistent with our previous study on LIF modeling [29] since the absorption cross-section of OH radical at 284 nm is on the order of one million times higher than the Rayleigh cross-section. This indicates that unlike LIF, the Rayleigh scattering imaging technique will enable visualizing the flow structure far from the detonation front.

The effect of the spatial distribution of the laser light intensity has been accounted for as described by Thiery et al. [47]. As seen in Figure 4 e), the Rayleigh intensity appears asymmetric, similar to what has been found for the LIF images [29]. This effect could be removed by performing a spatially-distributed normalization. While in the case of the LIF process, the intensity of the incident light is usually not known, the Rayleigh signal is not zero ahead of the detonation front and could be used to account for the intensity spatial distribution.

The effect of the dynamic range of the camera detector has been investigated considering a saturation level (well depth) of 20 e^-/px and a dark current of 10 e^-/px for a total number of levels of 256 (8 bits). It is seen in Figure 4 f) that using a camera with a too low dynamic range can lead to inconsistent features since some pockets of gas with average density located away from the detonation front might appear as dense as gas located just at the detonation front. A low dynamic range also tends to make the small scales disappear.

Figure 5 compares the experimental image of Anderson and Dabora [12] with the numerical Rayleigh intensity map. In order to obtain the closest agreement between the experimental and the numerical images, a number of features of the imaging system had to be accounted for. Anderson and Dabora used a 8 bit camera with pixel size of 70x70 μm and they performed an averaging over 10 pixels to reduce the noise of the image. As seen in Figure 5, the calculated Rayleigh

intensity map compares well with the experimental image once the actual parameters of the imaging system are accounted for. A number of features observed in the experiment are well represented such as the localized very high intensity at the triple points and the high intensity regions located behind the front between two diverging transverse waves. The length of the region of high intensity behind the incident shock is over-estimated in the simulation. This can be due to the higher dilution with Ar in the simulation than in the experiment; this makes the reaction zone appear longer.

3.3 Rayleigh intensity profiles

A quantitative comparison between the experimental Rayleigh scattering intensity profiles from Anderson and Dabora [12] and the calculated profiles has been performed. Both steady one-dimensional detonation (ZND model) [38], with velocities in the range D/D_{CJ}=0.85-1.2, and unsteady two-dimensional simulations have been considered for this comparison. D_{CJ} refers to the so-called Chapman-Jouguet velocity, i.e. the theoretical velocity of detonation wave. For the 2-D results, profiles have been taken at two locations as shown in Figure 4 a). It is seen in Figure 6 b) that the maximum Rayleigh intensity predicted by the ZND model at D_{CJ} lies in between the experimental values obtained at different locations of the detonation front. The intensity far from the detonation front is well reproduced. The width of the Rayleigh peak appears much thinner in the ZND simulation than in the experiments. These discrepancies between the experimental and calculated Rayleigh profiles are essentially due to the simplified description of the detonation wave structure considered in the ZND model. The experimental profiles have been obtained at different instants of the cellular cycle and thus for different shock velocities and shapes (curvatures). In order to account for the effect of velocity change, the Rayleigh intensity has been calculated for several velocities around the Chapman-Jouguet velocity as shown in Figure 6 a) for D/D_{CJ}=0.85 and c) for D/D_{CJ}=1.2. Concerning the peak intensity, the calculation performed for an over-driven ZND detonation is closer to the value measured behind the triple point (blue line) (Figure 6 c)) whereas for the calculation made for the under-driven case Figure 6 a), it is closer to the experimental value measured behind the flat leading shock (red line). Nevertheless, the intensity far from the front is shifted above the experimental value for the ZND simulation at D/D_{CJ}=1.2. The width of the ZND Rayleigh intensity peak is much smaller than the experimental observations independent of the velocity of the ZND detonation. The density jump across the one-dimensional shock is not very sensitive to velocity changes within

the range we considered. This result is consistent with Anderson and Dabora observations. In order to match their lowest experimental density jump values, they had to consider a one-dimensional detonation propagating at half the Chapman-jouguet velocity, D/D_{CJ}=0.5. This value seems quite low as compared to previous experimental [11] and numerical results [48, 49] which report a lowest detonation speed of D/D_{CJ}=0.7 within a cellular cycle. In order to match the highest density jump values they measured, Anderson and Dabora considered the density ratio resulting from the interaction of two opposing weak transverse waves. This indicates that the multi-dimensional structure of detonation waves has to be accounted for to obtain meaningful comparisons with Anderson and Dabora's measurements. For instance, the Rayleigh intensity profiles extracted from two-dimensional simulations obtained previously by Mével et al. [29] better match the experimental results as seen in Figure 6 d). Note that the conditions differ between the experiment, P_1=37.4 kPa, T_1=295 K, $2H_2$-O_2-4Ar, and the simulation, P_1=20 kPa, T_1=295 K, $2H_2$-O_2-12Ar. Concerning the peak intensity, the comparison is satisfactory for the leading shock outline whereas the peak intensity at the triple point is under-estimated by 20% by the simulation. This can be explained by the fact that the experimental intensity was taken just after the merging of two triple points, whereas the calculated one was taken just before collision of the two triple points. The width of the Rayleigh peaks is well reproduced by the simulation. On the contrary, the Rayleigh intensity away from the detonation front is over-estimated in the numerical simulation both at the incident shock and the triple point location.

3.4 Possible applications of Rayleigh imaging

Since the study of Anderson and Dabora has been performed, imaging systems have been much improved, notably in terms of resolution and dynamic range. The present approach could be used for designing a better imaging system and access a larger range of physical and chemical length scales. This is illustrated in Figure 7 a) for which a PCO2000 CDD camera, available in our laboratory [50], was considered for obtaining the Rayleigh intensity images. The resolution taken into account was 7x7 μm (with averaging, the resolution is 70x70 μm), and dynamic range of 14 bits (16384 levels of intensity). The image is much better resolved than in Anderson and Dabora's pioneering study and a much larger range of length scale can be observed both at and behind the detonation front. The increased spatial resolution of modern cameras might also enable direct measurement of the induction zone length. The evolution of the density within the detonation front can

be divided into three phases: (i) as the fresh mixture is shocked, a large density jump is observed; (ii) the density remains essentially constant within the induction zone during the radical pool build-up; and (iii) the density drops sharply as the exothermic step of the chemical process is taking place. Considering induction lengths on the order of 500 to 1000 μm and a spatial resolution of the imaging system (projected back to the object plane) of 30 μm, spatially resolved density profiles containing 20 to 30 points could be obtained. Such an approach could enable quantitative validation of detonation simulations as well as of detailed reaction models.

The possibility of using the Rayleigh scattering imaging technique to study the dynamics of the flow away from the detonation front is illustrated in Figure 7 b). The Rayleigh intensity map has been calculated from previous results obtained for a very lean H_2-N_2O mixture [41]. The particular feature of this image is the presence of large zones of gas with high Rayleigh intensity far from the detonation front. These zones correspond to isolated "islands" or "pockets" of unburnt gases which are reacting at a much slower rate. Such features have been observed mostly in mixtures with high activation energy but have also been reported for near-limit detonations [11, 51]. A numerical study by Gamezo et al. [52] demonstrated that the shape and consumption mechanism of the pockets depend on the activation energy of the mixture. For low activation energy mixtures, regular triangular-shaped pockets are observed and undergo auto-ignition. Mixtures with high activation feature pockets of irregular shape which are consumed through mixing with the surrounding burnt gases. Sharpe's [53] numerical investigation pointed out the influence of numerical resolution on the reaction rate within the unburnt pockets of gas which seems to indicate that diffusion plays an important role in their consumption process. These pockets are very difficult to visualize. Most experimental studies have been performed using the schlieren technique and, because of the integrating nature of this method, very narrow channels [51, 54]. Narrow channels are known to inducing a change of the detonation wave structure [55], by increasing the strength of the transverse waves, as well as large velocity deficits [11]. Previous studies have shown the importance of the strength of transverse shock waves in the formation and consumption of the unburnt gas pockets downstream of the detonation front, which makes the results of narrow channel experiments significantly different than tests in large channels. The LIF technique is not applicable to the study of unburnt pockets because little or no fluorescence signals originate from these regions which will appear as "dark patches" downstream of the detonation front [11]. Consequently, much remains unknown about

11

the dynamics and role in detonation propagation mechanism of these pockets. The specific chemical pathways, the role of convective and diffusive mixing processes, as well as the importance of the delayed local energy release taking place within these pockets and at interfaces, is unclear. Rayleigh scattering imaging could enable observing these pockets and improve our understanding of the dynamics of unstable and near-limits detonation waves.

4   Conclusion

Quantum chemistry has been employed to determine the Rayleigh cross-section of a large number of gaseous molecules. The database has been validated with respect to a variety of experimental data available in the literature. For most species, relative errors smaller than 10% was found. A wavelength dependent relationship for the variation of the Rayleigh scattering cross-section with temperature has been established based on previous experimental observations.

Rayleigh intensity profiles and synthetic images were calculated using steady 1-D and unsteady 2-D numerical simulations of detonations, and compared to the experimental results from Anderson and Dabora. Reasonable agreement was found for the Rayleigh peak height and width in the case of the 2-D simulations. A number of practical limits of the imaging system have to be accounted for in order to reproduce the experimental images. The present approach, which combines realistic chemistry, fluid dynamics, spectroscopy and imaging system effects, was demonstrated to be suitable to estimate the performance of a contemporary imaging system. Rayleigh scattering appears to be an appropriate technique to studying the structure of detonation waves both close to and far behind the front, and for providing reliable experimental data for the quantitative validation of detonation simulations performed with detailed chemistry.

The application of the present model to detonation propagating in hydrocarbon-based mixtures would require significantly extending the Rayleigh scattering cross-section database due to the large number of chemical species involved in hydrocarbons combustion. In the case of sufficiently rich mixtures, the Rayleigh signal may be significantly perturbed due to Mie scattering by soot.

Acknowledgements

References

[1] J. H. S. Lee, The Detonation Phenomenon, Cambridge University Press, 2008.

[2] B. Lewis, G. Von Elbe, Combustion, flames and explosions of gases., Academic Press Inc., London, 1961.

[3] J. E. Shepherd, Proceedings of the Combustion Institute 32 (2009) 83–98.

[4] D. R. White, Physics of Fluids 4 (1961) 465–480.

[5] D. R. White, G. E. Moore, Symposium (International) on Combustion 10 (1965) 785–795.

[6] A. K. Oppenheim, P. A. Urtiew, F. J. Weinberg, Proceedings of the Royal Society of London 291 (1966) 279–290.

[7] P. A. Urtiew, A. K. Oppenheim, Proceedings of the Royal Society of London. Series A, Mathematical and Physical Sciences 295 (1966) 13–28.

[8] R. I. Soloukhin, Shock waves and detonation in gases, Fizmatgiz, 1963.

[9] A. K. Oppenheim, Philosophical Tansactions of the Royal Society of London A 315 (1985) 471–508.

[10] F. Pintgen, Laser-optical visualization of detonation structures., Master's thesis, Technische Universitat Munchen-California Institute of Technology, 2000.

[11] J. M. Austin, The role of instability in gaseous detonation, Ph.D. thesis, California Institute of Technology, 2003.

[12] T. J. Anderson, E. K. Dabora, Symposium (International) on Combustion 24 (1992) 1853–1860.

[13] T. J. Anderson, A study of the structure of gaseous detonation waves using Rayleigh scattering, Ph.D. thesis, University of Connecticut, 1992.

[14] Y.-Q. Wen, Y.-K. Ye, N. Yan, Combustion, Explosion, and Shock Waves 48 (2012) 209–213.

[15] R. B. Miles, W. R. Lempert, J. N. Forkey, Measurement Science and Technology 12 (2001) R33.

[16] N. M. Laurendeau, Progress in Energy and Combustion Science 14 (1988) 147 – 170.

[17] F.-Q. Zhao, H. Hiroyasu, Progress in Energy and Combustion Science 19 (1993) 447 – 485.

[18] E. Kristensson, A. Ehn, J. Bood, M. Aldén, Proceedings of the Combustion Institute 35 (2015) 3689 – 3696.

[19] R. Barlow, G.-H. Wang, P. Anselmo-Filho, M. Sweeney, S. Hochgreb, Proceedings of the Combustion Institute 32 (2009) 945 – 953.

[20] R. Hanson, Symposium (International) on Combustion 21 (1986) 1677–1691.

[21] K. Kohse-Hoinghaus, R. S. Barlow, M. Alden, J. Wolfrum, Proceedings of the Combustion Institute 30 (2005) 89 – 123.

[22] M. Kamel, C. Morris, I. Stouklov, R. Hanson, Symposium (International) on Combustion 26 (1996) 2909 – 2915.

[23] C. Viguier, A. Gourara, D. Desbordes, Symposium (International) on Combustion 27 (1998) 2207 – 2214.

[24] G. Wang, C. Ma, B. Wang, Q. Lin, Chinese Science Bulletin 54 (2009) 2247–2255.

[25] J. M. Austin, F. Pintgen, J. E. Shepherd, Proceedings of the Combustion Institute 30 (2005) 1849–1857.

[26] F. Pintgen, Detonation diffraction in mixtures with various degrees of instability, Ph.D. thesis, California Institute of Technology, 2004.

[27] F. Pintgen, C. A. Eckett, J. M. Austin, J. E. Shepherd, Combustion and Flame 133 (2003) 211–229.

[28] F. Pintgen, J. E. Shepherd, Combustion and Flame 156 (2009) 655–677.

[29] R. Mével, D. Davidenko, J. Austin, F. Pintgen, J. E. Shepherd, International Journal of Hydrogen Energy 39 (2014) 6044–6060.

[30] W. Pitts, T. Kashiwagi, Journal of Fluid Mechanics 141 (1984) 391–429.

[31] L. Ponty, Application de la diffusion Rayleigh induite par laser a la caracterisation des fronts de flamme laminaire de premelange H_2/CH_4/Air et H_2/CO/Air, Ph.D. thesis, Universite d'Orleans, 2011.

[32] M. J. Frisch, G. W. Trucks, H. B. Schlegel, G. E. Scuseria, M. A. Robb, J. R. Cheeseman, J. A. Montgomery, T. Vreven, K. N. Kudin, J. C. Burant, J. M. Millam, S. S. Iyengar, J. Tomasi, V. Barone, B. Mennucci, M. Cossi, G. Scalmani, N. Rega, G. A. Petersson, H. Nakatsuji, M. Hada, M. Ehara, K. Toyota, R. Fukuda, J. Hasegawa, M. Ishida, T. Nakajima, Y. Honda, O. Kitao, H. Nakai, M. Klene, X. Li, J. E. Knox, H. P. Hratchian, J. B. Cross, V. Bakken, C. Adamo, J. Jaramillo, R. Gomperts, R. E. Stratmann, O. Yazyev, A. J. Austin, R. Cammi, C. Pomelli, J. W. Ochterski, P. Y. Ayala, K. Morokuma, G. A. Voth, P. Salvador, J. J. Dannenberg, V. G. Zakrzewski, S. Dapprich, A. D. Daniels, M. C. Strain, O. Farkas, D. K. Malick, A. D. Rabuck, K. Raghavachari, J. B. Foresman, J. V. Ortiz, Q. Cui, A. G. Baboul, S. Clifford, J. Cioslowski, B. B. Stefanov, G. Liu, A. Liashenko, P. Piskorz, I. Komaromi, R. L. Martin, D. J. Fox, T. Keith, A. M. A. Laham, C. Y. Peng, A. Nanayakkara, M. Challacombe, P. M. W. Gill, B. Johnson, W. Chen, M. W. Wong, C. Gonzalez, J. A. Pople, Gaussian 03, Revision C.02, 2003.

[33] W. C. Gardiner, Y. Hidaka, T. Tanzawa, Combustion and Flame 40 (1981) 213–219.

[34] J. Fielding, J. H. Frank, S. A. Kaiser, M. D. Smooke, M. B. Long, Proceedings of the Combustion Institute 29 (2002) 2703–2709.

[35] J. A. Sutton, J. F. Driscoll, Optics Letters 29 (2004).

[36] S. C. Graham, A. J. Grant, J. M. Jones, AIAA Journal 12 (1974).

[37] U. Holm, K. Kerl, Molecular Physics 58 (1986) 541–550.

[38] S. Kao, J. E. Shepherd, Numerical solution methods for control volume explosions and ZND detonation structure, Technical Report FM2006.007, GALCIT, 2008.

[39] G.-S. Jiang, C.-W. Shu, Journal of Computational Physics 126 (1996) 202–228.

[40] X. Zhong, Journal of Computational Physics 128 (1996) 19–31.

[41] D. Davidenko, R. Mével, G. Dupré, Shock Waves 21 (2011) 85–99.

[42] R. Mével, S. Javoy, F. Lafosse, N. Chaumeix, G. Dupré, C. E. Paillard, Proceedings of The Combustion Institute 32 (2009) 359–366.

[43] R. Mével, S. Javoy, G. Dupré, Proceedings of The Combustion Institute 33 (2011) 485–492.

[44] S. Javoy, R. Mével, G. Dupré, Chemical Physics Letters 500 (2010) 223–228.

[45] R. Mével, Etude de mécanismes cinétiques et des propriétés explosives des mélanges hydrogène-protoxyde d'azote et silane-protoxyde d'azote. Application à la sécurité industrielle, Ph.D. thesis, Université d'Orléans, 2009.

[46] N. T. Clemens, Encyclopedia of Imaging Science and Technology (2002).

[47] L. Thiery, J. Prenel, R. Porcar, Optics Communications 123 (1996) 801–809.

[48] C. A. Eckett, Numerical and analytical studies of the dynamics of gaseous detonations, Ph.D. thesis, California Institute of Technology, 2001.

[49] V. N. Gamezo, D. Desbordes, E. S. Oran, Combustion and Flame 116 (1999) 154–165.

[50] J. S. Damazo, Planar Reflection of Gaseous Detonations, Ph.D. thesis, California Institute of Technology, 2013.

[51] V. Subbotin, Fizika Goreniya i Vzryva 11 (1975) 96–102.

[52] V. N. Gamezo, D. Desbordes, E. S. Oran, Shock Waves 9 (1999) 11–17.

[53] G. Sharpe, Journal of Fluid Mechanics 447 (2001) 31–51.

[54] E. Oran, T. Young, J. Boris, J. Picone, D. Edwards, Symposium (International) on Combustion 19 (1982) 573–582.

[55] R. A. Strehlow, A. J. Crooker, Acta Astronautica 1 (1974) 303–315.
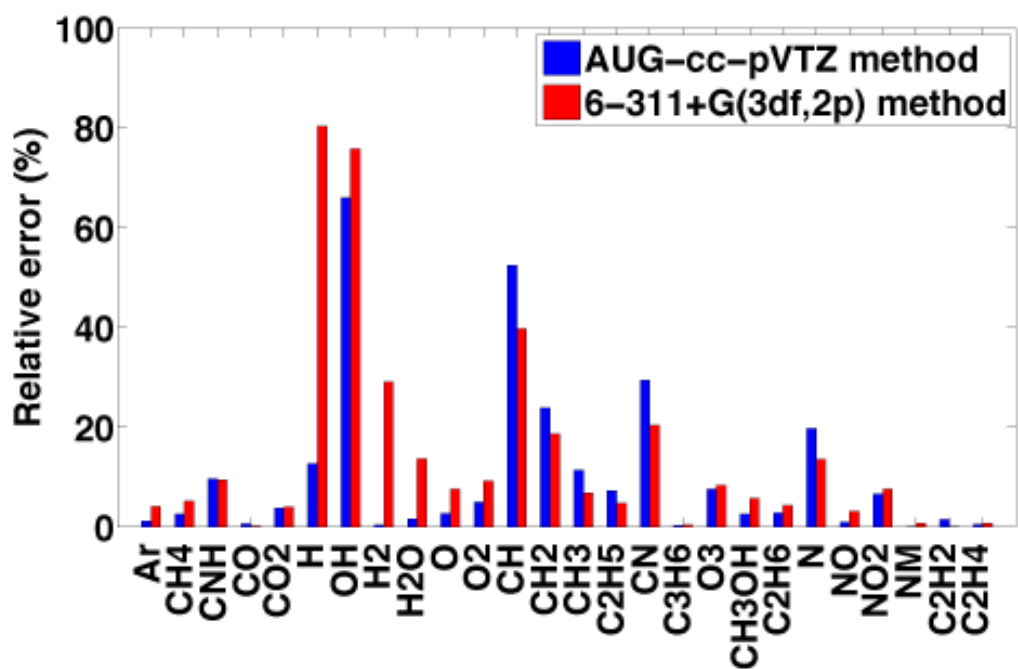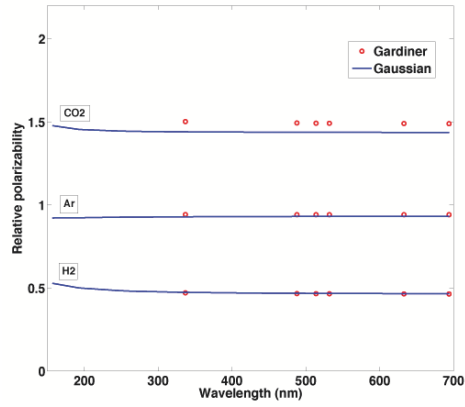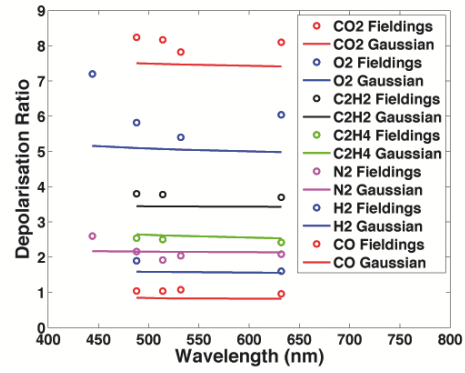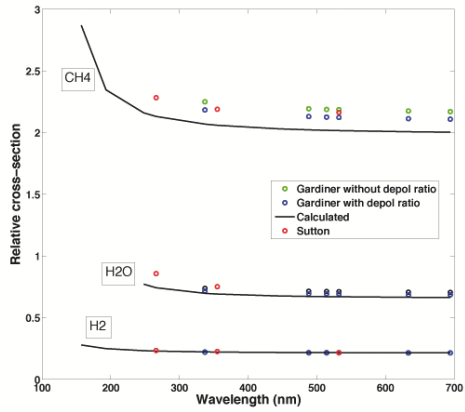
Figure captions

Figure 1: Comparison between Gardiner et al. [33] refractivity values and *Gaussian* values for the two basis sets.

a) Polarizabity for CO_2, Ar and H_2 [33]

b) Depolarization ratio [34]

c) Relative cross-section for H_2, H_2O and CH_4 [33, 35]

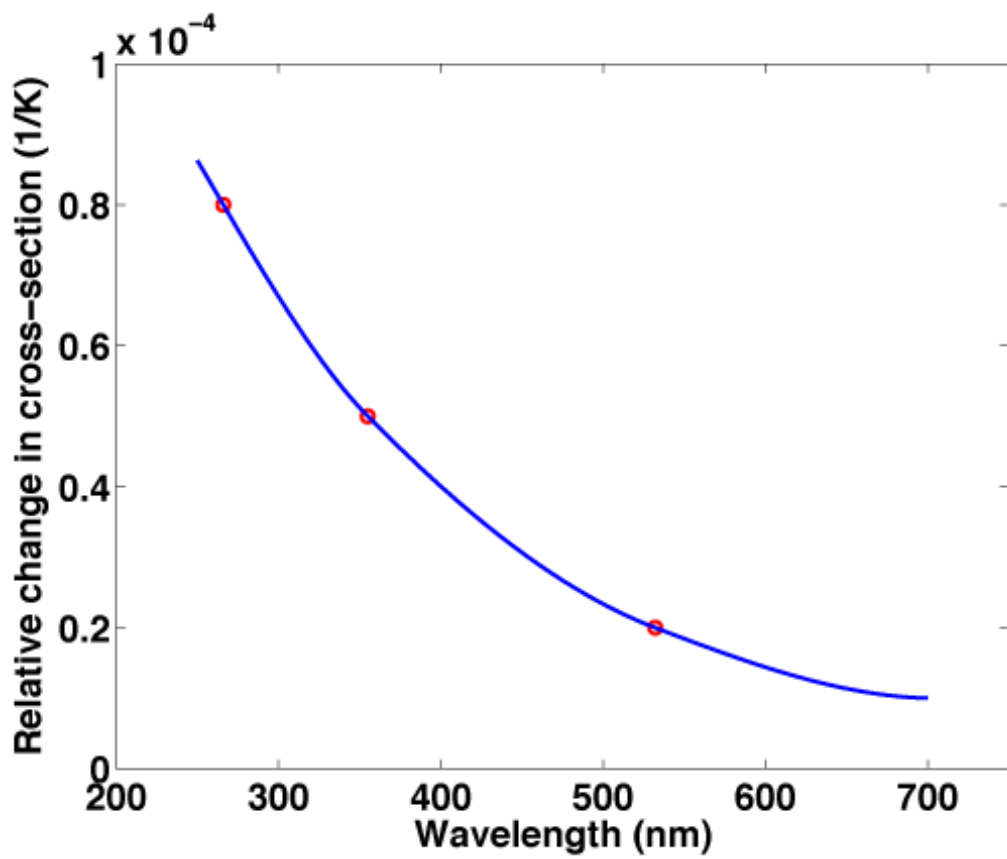Figure 2: Validation of the database against experimental data from the literature [33–35].

Figure 3: Assumed relative change of the Rayleigh scattering cross-section due to the temperature as a function of incident light wavelength. Estimation based on [17, 35–37].

a) Base image

b) Resolution

c) Averaging

d) Laser attenuation

e) Spatial distribution

f) Dynamic range
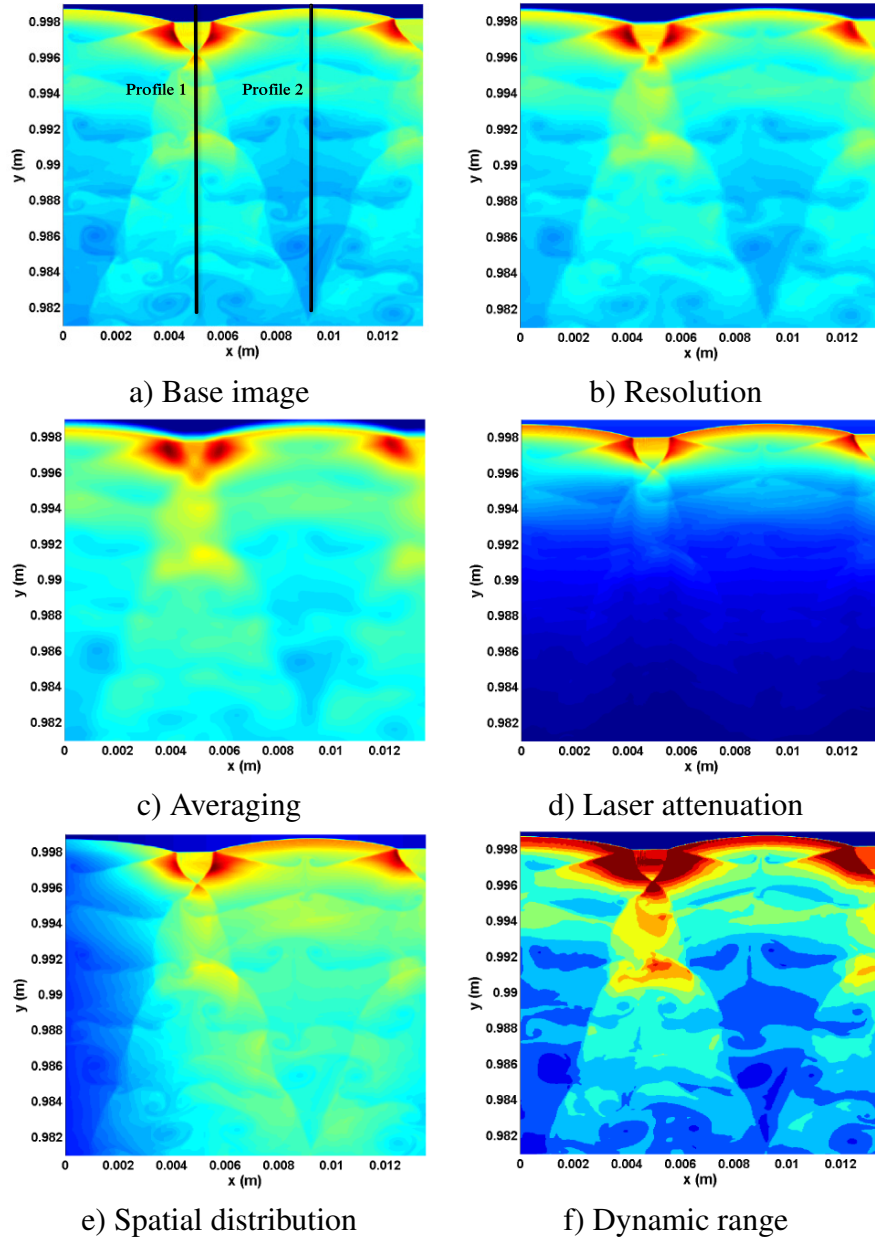
Figure 4: Effects of the characteristics of the imaging system on the Rayleigh scattering map of a detonation wave. Conditions: $2H_2$-O_2-12Ar; P_1=20 kPa; T_1=295 K. b) Resolution=70×70 μm; c) Averaging over 10 px; d) Laser attenuation: cross-section multiplied by 1×10^6; e) Spatial distribution: gaussian distribution as calculated from [47]; f) Dynamic range: saturation=20 e$^-$/px, dark current=10 e$^-$/px, 256 levels.

a) Experimental Rayleigh image   b) Numerical Rayleigh image

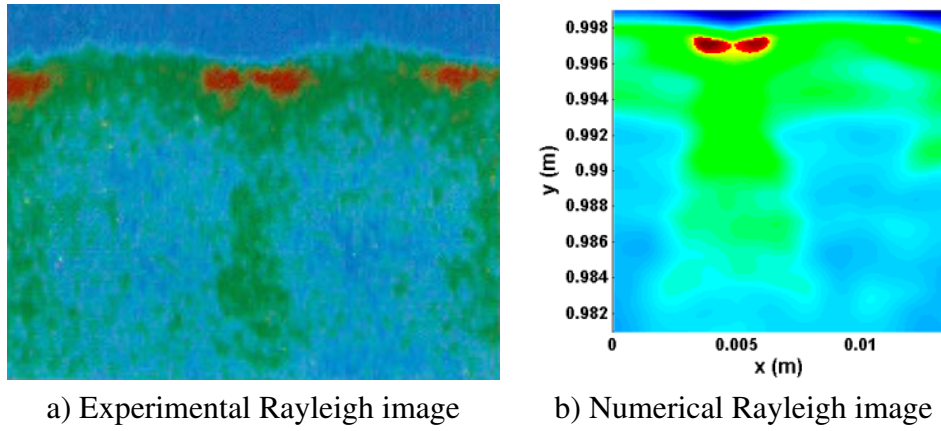Figure 5: Comparison between experimental [12] and numerical Rayleigh images of a detonation wave propagating in H_2-O_2-Ar mixtures. Conditions a): $1.2H_2$-O_2-3.76Ar; P_1=37.9 kPa; T_1=ambient. Conditions b): $2H_2$-O_2-12Ar; P_1=20 kPa; T_1=295 K.

a) D/D_{CJ}=0.85

b) D/D_{CJ}=1

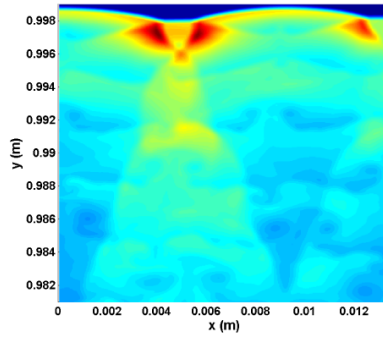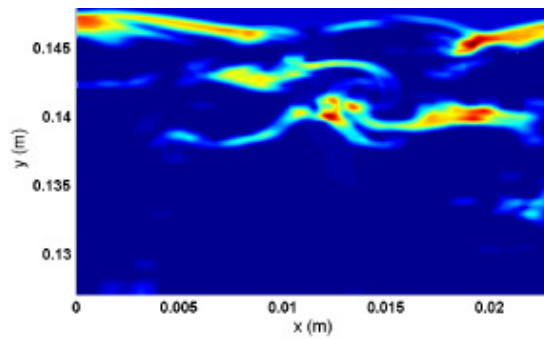c) D/D_{CJ}=1.2

d) Intensity profiles from 2-D simulation
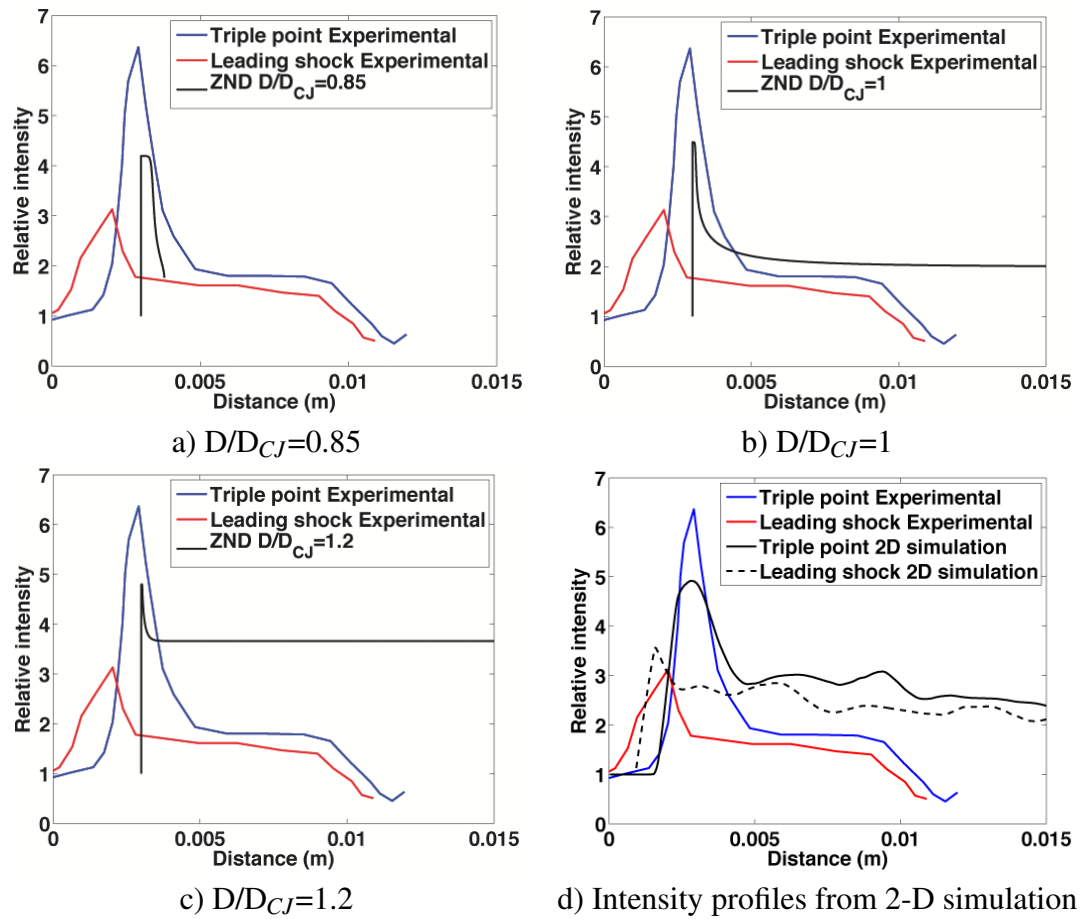
Figure 6: Comparison between experimental [12] and calculated Rayleigh intensity from ZND, a) to c), and 2-D, d), simulations. Conditions for experiments and ZND simulations: $1.2H_2$-O_2-$3.76Ar$; P_1=37.9 kPa; T_1=ambient. Conditions for 2-D simulations: $2H_2$-O_2-$12Ar$; P_1=20 kPa; T_1=295 K.

a) Rayleigh image expected with a PCO2000 CDD camera

b) Numerical Rayleigh image for a very lean H_2-N_2O mixture

Figure 7: Examples of numerical Rayleigh images of detonation waves which could be obtained with a modern imaging system. Conditions a): $2H_2$-O_2-$12Ar$; P_1=20 kPa; T_1=295 K. Conditions b): H_2-$14.4N_2O$; P_1=70.9 kPa; T_1=295 K.